Optik 166 (2018) 257–269

Contents lists available at ScienceDirect

Optik

journal homepage: www.elsevier.de/ijleo

Original research article

Vertical versus planar pulsed photoconductive antennas that emit in the terahertz regime

E. Moreno [a,*], R. Sohrabi [b], G. Klochok [c], E.A. Michael [a]

[a] Photonics Group, University of Chile, Chile
[b] Malek Ashtar University Of Technology, Isfaham, Iran
[c] Moscow State University Of Civil Engineering

ARTICLE INFO

Article history:
Received 12 December 2017
Received in revised form 24 March 2018
Accepted 26 March 2018

Keywords:
LT-GaAs
Simulations
Modeling
Terahertz source
Photoconductive antenna
Uni-traveling carriers
Mesa structures
Plasmonics

ABSTRACT

The design process of a photoconductive antenna (PCA), which emits efficiently in the electromagnetic terahertz range, demands some considerations that are discussed through this work. In this work, several essential characteristics of a photoconductive antenna made with LT-GaAS are studied by means of well established commercial software (COMSOL 5.3 [1]). An approach to the efficiency is also made through the study of geometry, the laser illumination position, the substrate doping distribution, the direction of the bias applied to the semiconductor, the matching impedance at the laser operating frequency and, finally, the plasmonics effects or penetration laser enhancement due to the use of nano antennas. We study and compare two kinds of structures, one which is quasi-bidimensional or planar and the other which is vertical. Additionally, the photoconductive antennas are also modeled by using a simplified equivalent circuit which helps to understand the antennas' performance. Therefore, some fundamental parameters, like the transient capacitance between the metal contacts are also studied. Furthermore, we introduce an optimized vertical design which achieves the best results.

© 2018 Elsevier GmbH. All rights reserved.

1. Introduction

Since the first pioneers attempted to accomplish the fabrication of powerful sources that radiate their power inside the terahertz band (0.1–10 THz), the accumulated knowledge has become huge. This fact has enabled great improvement in the area of power emitted in the THz band, although in 2012 the community was still suffering from non-efficient emitters [2].

To mend this, a particular kind of emitter, the so-called photoconductive, has caught the attention of many researchers, who are currently concerned with its efficiency due to its characteristics. One of the most important factors in the building up of efficient terahertz commercial devices is simplicity, which means a non-prohibitive cost. From this point of view photoconductive antennas represent a serious and realistic choice. For instance, simple sputtering techniques have been shown to enhance the efficiency around 7% [5]. In this paper the majority of geometrical features of the antennas studied are bigger than those explained in [5], so atomic layer deposition is not indispensable in our designs. However, the geometry and features of materials which compose the vertical structures could be fabricated by taking advantage of atomic layer deposition techniques.

* Corresponding author.
E-mail address: enrique@moreno.ws (E. Moreno).

https://doi.org/10.1016/j.ijleo.2018.03.096
0030-4026/© 2018 Elsevier GmbH. All rights reserved.

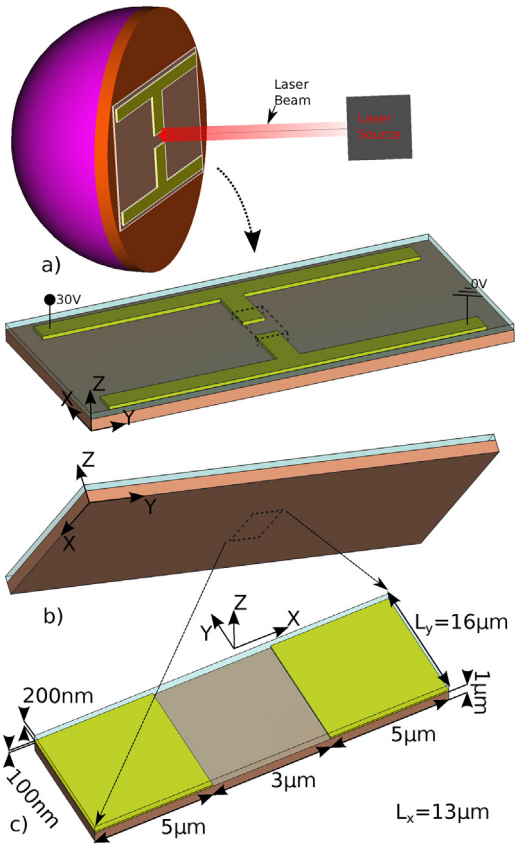

Fig. 1. (a) An entire planar PCA. (b) The figure corresponds to the part of a PCA which experiments the photoelectric effect (called photo-zone [3]). It is a composition of a semiconductor substrate, deposited metal contacts on that substrate and a layer of air that covers this photo-zone. (b) In [4] clearly shows what part of the PCA is commented in here. (c) Likewise the figure taken from the photo-zone denotes the particular area where the laser impinges the semiconductor and where the strongest photocurrent occurs. This is the gap between the metal contacts that bias the semiconductor, the core of the antenna. (The figures are not drawn to scale.)

In the present manuscript, aiming to investigate efficiency, we analyze the laser absorption rate into the semiconductor. Therefore, we exploit the plasmonics effects. These effects were a significant breakthrough [6] which permit a higher level of laser absorption in the semiconductor. Another meaningful parameter which has been considered here is a non-uniform doping distribution in the semiconductor [7,8]. In particular, unitraveling-carrier (UTC) photodiodes which are devices that employ an innovative distribution of the doping [7]. In the frequency domain, the UTCs play an important role because they can increase the higher frequency components that compose the photocurrent [7] and, consequently, the desirable frequencies which constitute the radiated field (Maxwell equations are linear). Moreover, the photo-Dember mechanism [9] is also taken into consideration.

A PCA is a non-linear device. Thus there are two types of impedance matchings. One is given by the antenna geometry and lens characteristics in order to improve the emission in the terahertz range and the other enhances the laser transmission into the semiconductor. The other is responsible for an intensification of the photoelectric effect and therefore the photocurrent. Accordingly anti-reflective coating has also been included in the vertical PCAs. Just the ones which show the best performance.

In addition, some publications that look upon the potential of plasmonics effects for enhancing the quantum efficiency of conventional ultrafast photoconductors do not take into account the electric bias direction of the semiconductor versus the laser focus spot position [10,11]. In [10] as well as in [11], Fig. 1 of these publications shows how the laser spot on the semiconductor is applied close to the anode. In those publications, the substrate was a uniform doping semiconductor, LT-GaAs. The photocurrent is obviously driven by holes or by slow electrons. This misconception is discussed here and the electric bias direction of the semiconductor versus the laser focus position is analyzed too.

Last but not least, the screening phenomenon [8] is scrutinized by virtue of the time dependent capacitance along the transient state. We make use of an equivalent circuit which helps to visualize and understand this phenomenon.

Figs. 1 and 2 illustrate both kinds of geometries studied. Their details are explained in Section 2.1. The paper has been structured in five sections. In Section 2 the computational domain under study is introduced together with all the parameters needed in the simulations carried out. In Section 3 all the simulations carried out along with an explanation that justifies them are described. Also, we compare the choice with several ones taken from literature in order to enrich our contribution. The

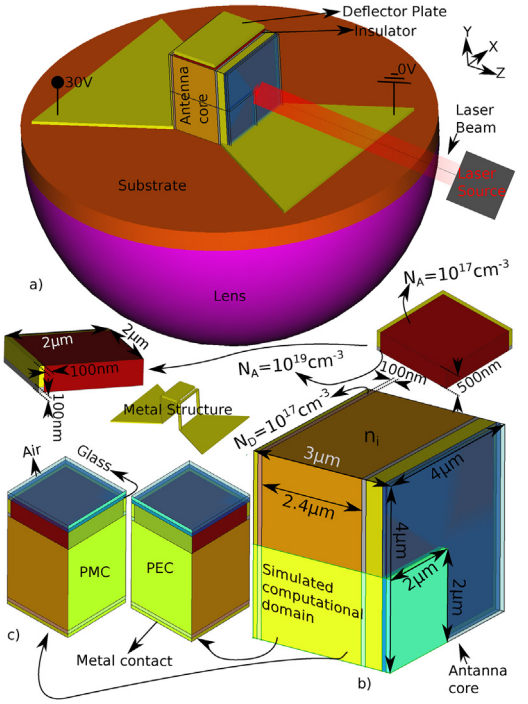

Fig. 2. (a) Entire vertical PCA. (b) The antenna core. (c) The simulated computational domain. It takes a quarter of the antenna core. Two planes of symmetry, a perfect electric conductor and a perfect magnetic conductor, allow this reduction in the computational domain.

circuit that models the PCA is presented in Section 4. Finally, Sections 5 and 6 correspond to the results and the conclusions, respectively.

2. Computational domain

A conventional planar PCA is depicted in Fig. 1(a) and (b) in Ref. [4] and it is also explained in detail there. Fig. 1(b) resembles the photo-zone defined in [3,4] which has already been successfully applied in studies focusing on the efficiency of a planar PCA [8]. However, the primary source of emission shown by the photo-zone portrayed in Fig. 1(b) is concentrated in a much smaller area, in the gap between the electrodes, which is illustrated in Fig. 1(c). In an analogous way, Fig. 2(a) shows a vertical PCA, where the so-called antenna core at the label on the figure, is detailed in Fig. 2(b). In fact, Fig. 2(b) is an equivalent gap to the photo-zone gap of a planar PCA (see Fig. 1(c)).

It is important to highlight that in the efficiency studies we do not face the usual multiscale problems [12,8,3,4]. Although it is true that there are currents far away from the gap displayed in Figs. 1(c) and 2(b), they are insignificant when compared with those within the gap. Besides this approximation, the foremost character which should be considered in the efficiency study is the radiated field. However, this magnitude is generated by the photocurrent in a linear form. This is because Maxwell's equations are linear, so the power radiated field is proportionally linear to the integration of the photocurrent density. Additionally, the Fourier transform is also linear, and the frequency composition of the radiated field is proportional to the frequency composition spectrum of the integrated current or photocurrent in the gap. In [8] we have extended the integration over the entire photo-zone. Nevertheless, the currents away from the gap are negligible if compared to the ones inside it. This, together with the necessity to establish a relative comparison between designs, leads us to restrict the integration to the transversal cross section of the gap. Hence, the photocurrent is calculated by integration over a virtual plane placed in the middle of the gap. It is an approach which is not new [11].

2.1. Designs

Under a geometrical point of view, the differences in planar PCA designs are fundamentally found in the gap which is illustrated in Fig. 1(c), where we have made some modifications (see Fig. 3). Analogously, the vertical PCA designs make reference to the gap exhibited in Fig. 2(b) in which a modification has been made in order to improve this first simple design (see Fig. 4). In total, we have simulated four planar and two vertical PCAs. Nevertheless, the number of simulations executed has been nine. With the exception of the planar UTC PCA simulated, all planar PCAs have been simulated twice: once in direct electric bias, that is, the laser spot is adjacent to the cathode and another time in reverse electric bias, in which case the laser spot is located close to the anode.

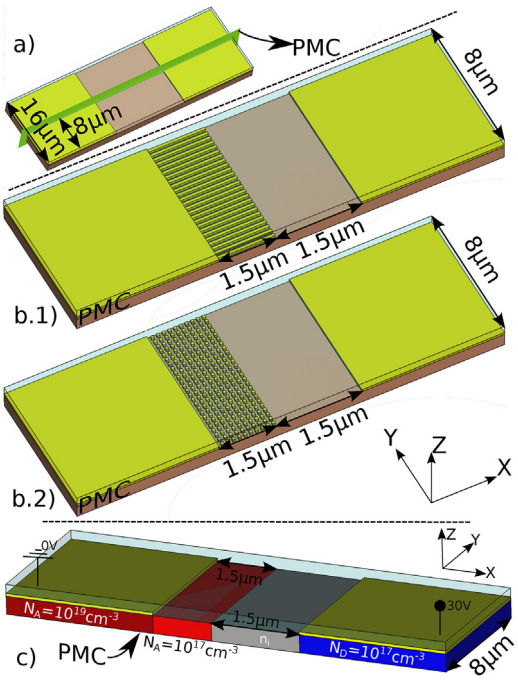

Fig. 3. (a) Gap of a simple planar PCA (see Fig. 1(c)) which has been reduced in half thanks to a perfect magnetic conductor plane (PMC). This reduces the computational cost by half. (b) Half gap of a comb shaped planar PCA. The comb shape is joined to the right side of the rectangular metal contact. (c) Half gap of an array of nano cubes deposited on a planar PCA. The array of nano cubes is deposited on the semiconductor close to one of the metal contacts and surrounded by air. (c) Half gap of a unitraveling-carrier planar PCA. (No scaling figures.)

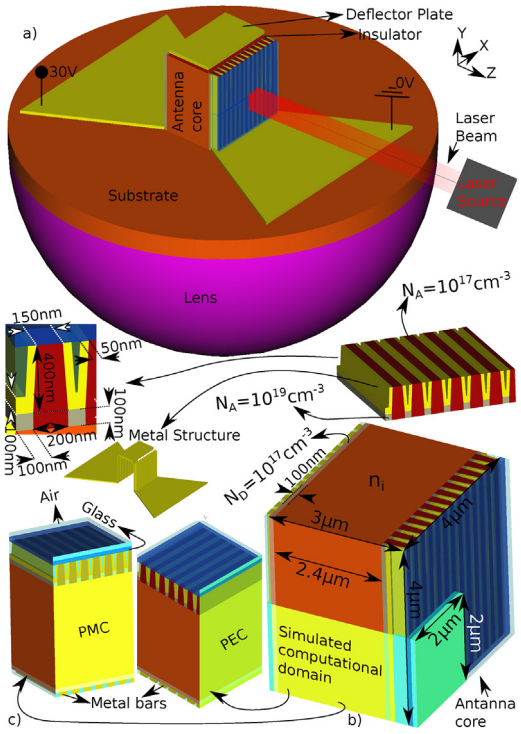

Fig. 4. The figure sketches an optimized vertical PCA. This device as well as the one displayed in Fig. 2 can be considered a vertical UTC PCA which uses the same doping distribution as a planar UTC PCA. This is a block barrier of acceptors $N_A = 10^{19}$ cm^{-3} layer under the cathode, a laser absorption layer of $N_A = 10^{17}$ cm^{-3}, an intrinsic spacer and the collector of electrons with $N_D = 10^{17}$ cm^{-3} on the anode. Its three-dimensional plasmonic structure has been taken from the planar PCA published in [5]. (a) Entire vertical PCA. (b) The antenna core. (c) Computational domain simulated. It is a quarter of the antenna core. Two planes of symmetry, a perfect electric conductor and a perfect magnetic conductor allow this reduction in the computational domain.

2.1.1. Planar PCAs

For planar PCAs, the computational domain applied to all simulations carried out in the present work are subscribed by the dashed hexahedron (D_{h2}) depicted in Fig. 1(b) which is amplified in Figs. 1(c) and 3(a). This first design is the simplest one. It has been already studied [13,12], and has both electrodes face to face keeping the rectangular shape depicted in 1(c) and 3(a). Hereinafter we will call this first design face-face (DFF). Indeed, we have simulated the half of the gap shown in 1(c) and 3(a). Fig. 3(a) reveals a perfect magnetic conductor (PMC) plane that has been computed as a functional mirror. This plane of symmetry allows realistic distributions of the laser electromagnetic fields in the considered domain. The PMC plane is employed in all planar PCAs simulated. By dividing the computational domain by half, we reduce the computational cost by half, which is a common practice [11].

The first design DFF is an exception, while the remaining ones are asymmetrical designs. The laser is applied on one side, just on the one which contains one of these things; nothing, bars or cubes as shown in Figs. 3(a), 3(b.1) and 3(b.2) respectively. The second design resembles a series of parallel bars joined to the right side of the rectangular metal contact shown in Fig. 3(a). This configuration looks like the comb shape displayed in Fig. 3(b.1). The series of bars are 1.5 μm long, 100 nm thick and wide, and are separated 100 nm from each other. The bars are attached to the original plain electrode, in such a way that it combines to the rectangular metal electrode and bias the semiconductor. Whereupon they can be considered an electrode part. This is the only case in which a design reduces the gap length to 1.5 μm. Something that does not produce a spectacular growth in the generated intensity of photocurrent when it is compared with other designs, in spite of the fact that the electric field is higher. Hereinafter we will call this second design comb-shape (DCS). The third design presented in Fig. 3(b.2) is associated with an array of nano cubes deposited on the semiconductor. Every cube has got 100 nm in side and it is separated 100 nm from its neighbors. Hereinafter we will call this third design with a layer of cubes (DLC).

The doping distribution in the semiconductor of a planar PCA is a fundamental parameter in relation to the efficiency achievable by that PCA [8,7]. We divide the studies carried out into two groups. In the first group we assume a semiconductor with a uniform doping distribution of donors $N_D = 10^{15}$ cm^{-3}. This doping distribution, which has already led to the worst efficiency in [8], is an excellent starting point in order to establish a relative comparison between designs under the same laser power condition as well as the same electric bias. The UTC means an improvement to the intrinsic semiconductor which presents the best performance [8,7]. So we have also simulated a planar UTC PCA free of any element in the gap, in short, a geometry DFF. This simulated planar UTC PCA is depicted in Fig. 3(c). Its doping distribution is $N_A = 10^{19}$ cm^{-3} for the block layer under the cathode, $N_A = 10^{17}$ cm^{-3} for the absorption layer, $N_D = 10^{17}$ cm^{-3} for the collector layer beneath the anode and an intrinsic spacer and the collector of electrons with beneath the anode.

2.1.2. Vertical PCAs

The vertical PCA fabrication could be a potential limitation for this technology, at least, whereas it is not reality. The only fact that legitimizes this technology is its existence in the real life. The vertical PCA fabrication, later testing and measurements is the only admissible proof. Having said that, we think that already the fabrication is possible. For instance, the DOV structure demands a resolution as accurate as 50 nm and currently nano-fabrication technology makes this possible already [14–17]. This issue is discussed deeper in the upcoming Section 2.2. Vertical PCA features take advantage and overcome a lot planar PCAs features as it is proved by the results obtained in the present work. On the one hand, none of the existing PCAs are free of photo-Dember effect [9], while on the other hand, photo-Dember effect is desirable in vertical UTC PCAs. In an UTC PCA the holes should be trapped by the cathode while the electrons are expected to cross the entire gap. The photocurrent in a PCA can be simplified by an equivalent dipole of current. In a vertical PCA there is not any orthogonal component of the equivalent dipole of current to the ideal flow of carriers. In a planar PCA the equivalent dipole of current has two components. An ideal component that follows the line which joins the cathode to the anode, and an undesirable component, which is due to the photo-Dember effect. In this set up the laser is applied to the semiconductor in a perpendicular direction to that line, and this is the reason for that undesirable vertical component of the equivalent dipole of current. In a vertical PCA, the laser propagation runs in the same direction as the ideal flow of carriers. For good measure, in a vertical PCA it is possible to add a metal plate to the back of the terahertz radiation direction. Figs. 2(a) and 4(a) give an accurate picture of this feature.

We have simulated two vertical UTC PCAs. The first one depicted in Fig. 2 has a square frame of metal that works as the cathode. The core of this frame is the laser absorption layer which has a doping of acceptors $N_A = 10^{17}$ cm^{-3}. Below the cathode there is a semiconductor frame with a concentration of impurities $N_A = 10^{19}$ cm^{-3}, which acts as a barrier for electrons. This semiconductor frame with a high rate of acceptors surrounds the core of semiconductor which operates as the laser absorption layer. Beneath these two doped semiconductors there is an intrinsic layer which functions as a spacer, just the same way as the intrinsic spacer in a PIN diode [18]. Finally, a layer of collectors doped with a concentration of donors $N_D = 10^{17}$ cm^{-3} is placed between the intrinsic layer and the anode. Hereinafter we will call this design a vertical simple (DVS).

The second vertical PCA simulated shares the main characteristics with the first one. In fact, there are only two differences, the anode is not a plate and the cathode is a geometrical variation of the three-dimensional plasmonic structure introduced in [5]. The details of this plasmonic structure are summarized in Fig. 2. The anode is made up of a series of bars which are

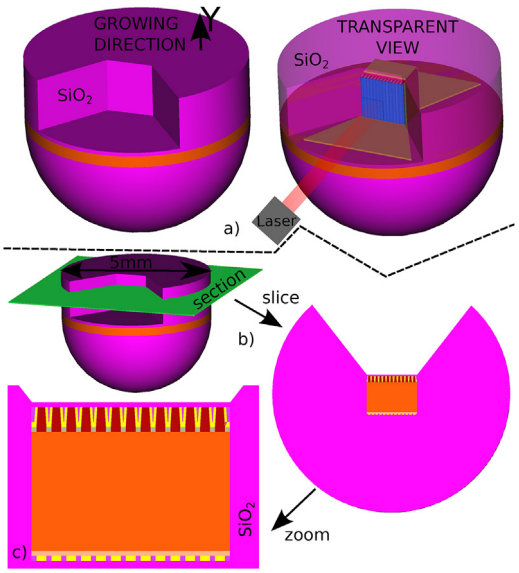

Fig. 5. (a) Real vertical PCA with its bulky encapsulation of SiO_2. (b) Transversal cross section of the antenna core plus its encapsulation. (c) It is a zoom of the antenna core encased by the encapsulation. This is a zoom of the transversal cross section sketched in (b).

100 nm thick and 200 nm wide. They are separated by 100 nm from one another. Hereinafter we will call this design a vertical optimized (DVO).

2.2. Robustness and matching impedance

Vertical designs are fabricated layer by layer in the direction indicated in Fig. 5. It is a misconception to guess a procedure in which the antenna substrate, lens and antenna arms are fabricated separately from the antenna core introduced in Figs. 2 and 4, and they are joined in a subsequent step of fabrication. This means a continuous process where the entire antenna, including its encapsulation, is fabricated. Kurt J. Lesker ALD-150LX which is able to combine sputtering and ALD due to its two chambers connected through a load-lock could be employed. For the sake of clarity, in Figs. 2 and 4, we have omitted the bulky encapsulation of SiO_2 that encases the antenna core. In addition to robustness and the oxidation prevention, the encapsulation acts as an anti-reflection coating of thin film 100 nm thick made with SiO_2 which improves laser absorption. For this encapsulation, a solid SiO_2 medium is presumed, but a medium with empty cavities and low K [19] could also be used. Therefore, the encapsulation should have a lower electric permittivity than the one without cavities inside hence it traps less quantity of radiated field. Anyway, in the studied vertical designs the directivity of radiation given by the main source-the photocurrent is not influenced by the encapsulation which should be considered as secondary sources after reflections in the back defector plate.

Finally we suggest a detailed fabrication procedure in [20].

3. Simulations

The simulations have been effectuated in COMSOL 5.3 commercial software [1] in two steps. In COMSOL there are two physical interfaces. The initial step is called “The Radio Frequency, Electromagnetic Waves, Frequency Domain” in COMSOL. Time-harmonic electromagnetic field distributions are solved by this interface. Therefore in the frequency domain we calculate the electric field distribution in the entire computational domain at the operational laser frequency by solving the Helmholtz equation (1) defined below.

The later step, called “Semiconductor” in COMSOL, deals with the transient process in the time domain by solving the Poisson equation (14) and continuity equations (15) and (16) which are defined in Section 3.2. This technique in which the drift-diffusion equations for electrons and holes model the semiconductor behavior has already been reported in many cases [21,13,12,3,11]. Here we incorporate some modifications to [11] which are explained in Sections 3.1 and 3.2.

3.1. Frequency domain

The generation rate function of charge carriers is modeled by the photoelectric effect which depends on the optical power $I(\vec{r})$. Accordingly, the generation rate function that is a result of the interaction between the monochromatic wave (the laser) and the semiconductor relies on the electric field distribution of the laser because $I(\vec{r}) = |\vec{E}\left(\vec{r}\right)|^2$ [22]. Consequently, it is

mandatory to determine the electric field distribution $\vec{E}(\vec{r})$ in the semiconductor. To do this, we firstly solve the Helmholtz equation,

$$\nabla \times \left(\nabla \times \vec{E}(\vec{r})\right) = \mu\omega^2 \varepsilon_{eq}(\omega)\vec{E}(\vec{r}) \tag{1}$$

where μ is the magnetic permeability and $\varepsilon_{eq}(\omega) = \varepsilon_r\varepsilon_0 - j\frac{\sigma}{\omega}$ is the electric permittivity.

In order to approach the Helmholtz equation, we consider two kinds of boundary conditions which partially enclose the computational domain and fix a unique solution; the physical one. The boundary condition located at the top surface of the computational domain determines the values of the electric field given by the laser source. Eq. (2) in [11] provides an infinite energy distribution of laser in the Y axes. Thus, we remodel the non realistic Gaussian beam source expressed by Eq. (2) in [11] with the subsequent equation

$$\vec{E}_{inc}(\vec{r}) = \hat{x}E_0 e^{2\ln(0.5)\left(\left(\frac{x-x_0}{\sigma_x}\right)^2 + \left(\frac{y-y_0}{\sigma_y}\right)^2\right)} \tag{2}$$

$$E_0 = \sqrt{\frac{8\eta_0 P_{ave}}{\nu_\gamma \sigma_x \sigma_y \sigma_t}}\left(\frac{\ln(2)}{\pi}\right)^{3/4} \tag{3}$$

For planar PCA this boundary condition in the top surface of the computational domain is the impedance boundary condition specified by Eq. (4). At the bottom ($z=0$), forward ($x=L_x$), backward ($x=0$) and left ($y=L_y/2$) surfaces that enclose the computational domain, we consider the impedance boundary condition without sources $\vec{E}_{inc} = \bar{0}$. Hence, these boundary conditions are a simplification of Eq. (4) which is transformed into Eq. (5). And, for vertical PCAs, the boundary condition in the top surface (see system of reference in Fig. 4(a)) of the computational domain is also the impedance boundary condition specified by Eq. (4). At the bottom ($z=0$), backward ($x=0$) and right ($y=0$) surfaces that enclose the vertical computational domain, we consider the impedance boundary condition given by Eq. (5).

$$\sqrt{\frac{\mu_0\mu_r}{\varepsilon_{eq}(\omega)}}\hat{n} \times \vec{H}\left(\vec{r}\right) + \vec{E}\left(\vec{r}\right) + \vec{E}_{inc}\left(\vec{r}\right) = (\hat{n} \cdot (\vec{E}\left(\vec{r}\right) + \vec{E}_{inc}\left(\vec{r}\right)))\hat{n} \tag{4}$$

$$\sqrt{\frac{\mu_0\mu_r}{\varepsilon_{eq}(\omega)}}\hat{n} \times \vec{H}\left(\vec{r}\right) + \vec{E}\left(\vec{r}\right) = (\hat{n} \cdot \vec{E}\left(\vec{r}\right))\hat{n} \tag{5}$$

$$\hat{y} \times \vec{H}(\vec{r}) = \bar{0} \tag{6}$$

$$\hat{x} \times \vec{E}(\vec{r}) = \bar{0} \tag{7}$$

For planar PCAs, at the right side ($y=0$) of the computational domain, by virtue of the expected symmetrical behavior, we impose a perfect magnetic conductor plane which is summarized by Eq. (6). In this way, for vertical PCAs, we employ two kinds of functional mirrors. On the left side ($y=L_y/2$) we apply a perfect magnetic conductor surface which is also specified by Eq. (6). Then on the forward side ($x=L_x/2$) we apply a perfect electric conductor surface which is designated in this case by Eq. (7).

Due to the hypothesis that the electric field has harmonic structure, the Poynting vector can be expressed as $\langle\vec{S}\rangle = \frac{Re(\vec{E}_0 \times \vec{H}_0^*)}{2}$. Along with this we can employ the expression $\vec{k} \times \vec{E} = \mu\omega\vec{H}$ so as to calculate the energy propagation in all canonical directions ($\hat{x}$, $\hat{y}$, $\hat{z}$) via Eqs. (8)–(10). The combination of these expressions leads to the optical power per unit of surface linked to a spherical wave of laser energy inside the semiconductor, which is given by Eq. (11).

$$\langle\vec{S}\rangle_{\vec{k}_x} = \frac{Re\left(|E_{oy}|^2 + |E_{oz}|^2\right)}{2\eta} \tag{8}$$

$$\langle\vec{S}\rangle_{\vec{k}_y} = \frac{Re\left(|E_{ox}|^2 + |E_{oz}|^2\right)}{2\eta} \tag{9}$$

$$\langle\vec{S}\rangle_{\vec{k}_z} = \frac{Re\left(|E_{ox}|^2 + |E_{oy}|^2\right)}{2\eta} \tag{10}$$

$$P_s = \sqrt{\left(\langle\vec{S}\rangle_{\vec{k}_x}\right)^2 + \left(\langle\vec{S}\rangle_{\vec{k}_y}\right)^2 + \left(\langle\vec{S}\rangle_{\vec{k}_z}\right)^2} \tag{11}$$

P_s can be contemplated as the peak of optical intensity over the transient simulation (the second step) and, in this way, as the instant of time when the charge generation rate achieves its maximum value. Here we correct two errata in [11]. One is the signs in Eqs. (4)–(6) in [11] and the other is a missing square root in Eq. (7) in [11].

3.2. Time domain

The quantum efficiency of the generation rate model is pondered by the extinction coefficient k_{PC} in Eq. (12). Inasmuch as $\frac{2k_{PC}P_s}{\hbar c}$ are the electron–hole pairs generated at the peak of generation.

$$G(\vec{r},t) = \frac{2k_{PC}P_s}{\hbar c} sech^2\left(\frac{1.76(t-t_0)}{\sigma_t}\right) \tag{12}$$

$$R(\vec{r},t) = \frac{n(\vec{r},t)p(\vec{r},t)}{\tau_n(p(\vec{r},t)+p1(\vec{r}))+\tau_p(n(\vec{r},t)+n1(\vec{r}))} + n(\vec{r},t)p(\vec{r},t)(n(\vec{r},t)C_n + p(\vec{r},t)C_p) \tag{13}$$

With regard to modeling of the generation rate time profile, we assume a squared hyperbolic secant function. Ultrashort pulses from mode-locked lasers often have a temporal shape which can be mathematically approximated by means of a squared hyperbolic secant function. This function has longer tails than Gaussian function. This is the reason because the squared hyperbolic secant function approximates the laser pulse over time more accurately than a Gaussian function [23]. Along with the source of charge carriers, there is sink of charge carriers, which is called recombination rate function (13). We use a Shockley-Read-Hall model which accounts Auger captures. Thus the net balance of charge carriers is defined as $GR(\vec{r},t) = G(\vec{r},t) - R(\vec{r},t)$.

In the continuity equation $\vec{\nabla}\cdot\vec{J}(\vec{r},t) = -\partial_t\rho(\vec{r},t)$ where $\rho(\vec{r},t) = q\left(p(\vec{r},t) - n(\vec{r},t) + N_D^+(\vec{r}) - N_A^-(\vec{r})\right)$ we presume that the density of current $\vec{J}(\vec{r},t)$ is modeled by the drift-diffusion. So the transient process is completely characterized thanks to the following system of partial differential equations.

$$\nabla\cdot\left(-\varepsilon_r\left(\vec{r}\right)\nabla V\left(\vec{r},t\right)\right) = \rho\left(\vec{r},t\right) \tag{14}$$

$$\partial_t n\left(\vec{r},t\right) = \nabla\left(\mu_n\left(\vec{r},t\right)\left(V_T\nabla n(\vec{r},t) - n\left(\vec{r},t\right)\nabla\left(V\left(\vec{r},t\right)+\chi\left(\vec{r}\right)\right)\right)\right) + GR\left(\vec{r},t\right) \tag{15}$$

$$\partial_t p\left(\vec{r},t\right) = -\nabla\left(\mu_p\left(\vec{r},t\right)\left(V_T\nabla p\left(\vec{r},t\right) + p\left(\vec{r},t\right)\nabla\left(V\left(\vec{r},t\right)+\chi\left(\vec{r}\right)+E_g\left(\vec{r}\right)\right)\right)\right) + GR\left(\vec{r},t\right) \tag{16}$$

COMSOL 5.3 enables the enrichment and accuracy of solution by using the Caughey-Thomas mobility model for carriers in the semiconductor (Table 1).

$$\mu_u(\vec{r},t) = \frac{\mu_{u,in}}{\left(1+\left(\frac{\mu_{u,in}|\nabla V(\vec{r},t)|}{v_{u,sat}}\right)^{\alpha_u}\right)^{1/\alpha_u}} \tag{17}$$

This model has already demonstrated its ability to refine the accuracy in fitting experimental data [13,8,12,3,4]. So this mobility model has been taken into consideration in all simulations. The parameters in Eq. (17), the Caughey-Thomas model, are listed in Table 2. In this equation the symbol u means both kinds of carriers, electrons $u = n$ and holes $u = p$. Obviously, the Helmholtz equation is solved first (Table 2). Its solution serves as the starting point in the transient stage which describes the semiconductor. In that second stage, the initial voltage distribution in the semiconductor is a simplification. A linear approximation in the gradient of voltage between the metal contacts at the gap is considered to be true in the starting instant of time $t = 0$. Also, the charge carriers are in equilibrium with this electric field distribution caused by the linear external bias.

3.3. List of simulations carried out

All the simulations share the same laser conditions and are biased by the same difference of electric potential. Even so, the disparities listed here are:

1. DFF (planar PCA)
   (a) Simulation (1) Direct bias (anode close to the spot laser) and a uniform doping which can be consulted in Table 2. In Figs. 7 and 8 this simulation is designated as DFF (a).
   (b) Simulation (2) Inverse bias (cathode close to the spot laser) and a uniform which can be consulted in Table 2. In Figs. 7 and 8 this simulation is designated as DFF (b).
   (c) Simulation (7) Direct bias, and UTC which can be consulted in Table 2. In Figs. 7 and 8 this simulation is designated as DFF (c).
2. DCS (planar PCA)
   (a) Simulation (3) Direct bias (anode close to the spot laser) and a uniform doping which can be consulted in Table 2. In Figs. 7–9 this simulation is designated as DCS (a).
   (b) Simulation (4) Inverse bias (cathode close to the spot laser) and a uniform concentration of donors which can be consulted in Table 2. In Figs. 7–9 this simulation is designated as DCS (b).

Table 1
Parameters and magnitudes' values for the first step where the Helmholtz equation is solved.

Description	Magnitude
Free-space wavelength	$\lambda = 780$ nm
Average laser power	$P_{ave} = 0.63$ mW
Laser pulse repetition rate	$\nu_\gamma = 80$ MHz
Pulse center location (time)	$t_0 = 3$ ps
Pulse HPBW (x direction)	$\sigma_x = 2$ μm
Pulse HPBW (y direction)	$\sigma_y = 2$ μm
Pulse FWHM (time)	$\sigma_t = 120$ fs
DC bias voltage	$V_0 = 30$ V
Metal contacts (Au)	$\tilde{\varepsilon}_r = -25.508 + 1.0236j$ [24]
Magnetic permeability	$\mu_r = 1$
Extinction coefficient	$k_{PC} = 0.0625$ [25]
Planar structures	
Laser x-axis center location	$x_0 = 6.0$ μm
Laser y-axis center location	$y_0 = 0.0$ μm
Uniform doping	
Semiconductor LT-GaAs	$\tilde{\varepsilon}_r = 13.657 + 0.006j$ [26]
Planar UTC	
LT-GaAs spacer	$\tilde{\varepsilon}_r = 13.657 + 1.33 \cdot 10^{-11} j$ [26]
LT-GaAs absorption	$\tilde{\varepsilon}_r = 13.657 + 0.03j$ [26]
LT-GaAs diffusion barrier	$\tilde{\varepsilon}_r = 13.657 + 3j$ [26]
LT-GaAs collector	$\tilde{\varepsilon}_r = 13.657 + 0.6j$ [26]
Vertical structures	
Laser x-axis center location	$x_0 = 2.0$ μm
Laser y-axis center location	$y_0 = 2.0$ μm
Thin layer of SiO_2 (100 nm)	$\tilde{\varepsilon}_{r,Glass} = 2.1698 + 0.0j$ [27]
LT-GaAs has the same values as planar UTC	

Table 2
Parameters and magnitudes values for the second stage where the Poisson equation coupled to the continuity equation is solved. Some parameter has been obtained from table B-24a in [28].

Description	Magnitude
Low-field electron mobility	$\mu_{n,in} = 8000 \frac{cm^2}{V\,s}$ [28]
Low-field hole mobility	$\mu_{p,in} = 400 \frac{cm^2}{V\,s}$ [28]
Bandgap	$E_g = 1.424$ eV [29]
Electrons affinity	$\chi = 4.07$ eV [29]
Temperature	$T = 293.15$ K
Conduction band density of states	$N_c = 4.35 \cdot 10^{17}$ cm^{-3} [28]
Valence band density of states	$N_v = 8.16 \cdot 10^{18}$ cm^{-3} [28]
SRH electron lifetime	$\tau_n = 0.3$ ps [30]
SRH hole lifetime	$\tau_p = 0.4$ ps [30]
Auger electron coefficient	$C_n = 5.0 \cdot 10^{-30} \frac{cm^6}{s}$ [28]
Auger hole coefficient	$C_p = 1.0 \cdot 10^{-31} \frac{cm^6}{s}$ [28]
p if Fermi level $E_F = E_{traps}$	$p_1 = 4.5 \cdot 10^6$ cm^{-3}
n if Fermi level $E_F = E_{traps}$	$n_1 = 4.5 \cdot 10^6$ cm^{-3}
Electron alpha coefficient (Eq. (17))	$\alpha_{n,0} = 1.82$ [28]
Hole alpha coefficient (Eq. (17))	$\alpha_{p,0} = 1.75$ [28]
Electron saturation velocity (Eq. (17))	$v_{n,sat} = 7.7 \cdot 10^6 \frac{cm}{s}$ [28]
Hole saturation velocity (Eq. (17))	$v_{p,sat} = 7.7 \cdot 10^6 \frac{cm}{s}$ [28]
Uniform doping in planar structures	
N_D^+ donor doping concentration	10^{15} cm^{-3}
Planar/vertical UTCs	
Diffusion barrier	$N_A^{--} = 10^{19}$ cm^{-3}
Laser absorption layer	$N_A^{-} = 10^{17}$ cm^{-3}
Spacer area	$n_i = 2.12 \cdot 10^6$ cm^{-3} [28]
Collector region	$N_D^{+} = 10^{17}$ cm^{-3}

3. DLC (planar PCA)
   (a) Simulation (5) Direct bias (anode close to the spot laser) and a uniform concentration of donors which can be consulted in Table 2. In Figs. 7 and 8 this simulation is designated as DLC (a).

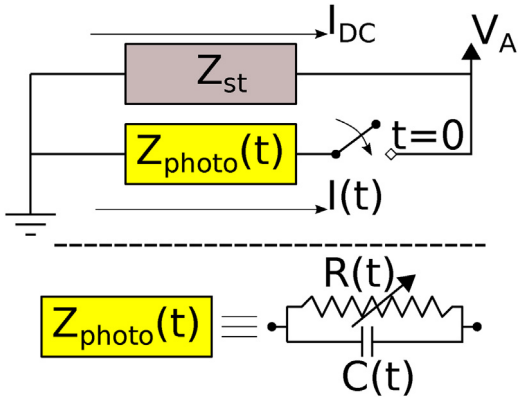

Fig. 6. Circuital model which reproduces a PCA.

(b) Simulation (6) Inverse bias (cathode near to the spot laser) and a uniform doping which can be consulted in Table 2. In Figs. 7 and 8 this simulation is designated as DLC (b).

4. DVS (vertical PCA)
   (a) Simulation (8) Direct bias, and vertical UTC portrayed in Fig. 2. Its details can be consulted in Table 2. In Figs. 7 and 8 this simulation is designated as DVS.
   (b) Simulation (9) Direct bias, and vertical UTC portrayed in Fig. 4. Its details can be consulted in Table 2. In Figs. 7 and 8 this simulation is designated as DVO.

4. Equivalent circuit and efficiency

The efficiency of a PCA is defined in [8]. Eq. (1) in [8] points out that efficiency is a relation between two terms. On the one hand we have the energy supplied to the PCA and on the other hand the energy radiated by the PCA. The energy supplied to the PCA is the sum of two terms, the energy provided by the laser and the energy given by the external electric source. We also assume that the radiated energy is proportional to the total current which flows in the gap. Bearing in mind that the energy provided by the laser is the same for all simulations, we can focus the study on the photocurrent generated as well as on the energy given by the external electric source, where the electric potential which biases the PCA has been kept constant. This second term is easily deemed when we avail ourselves of a simplified circuit model for the PCA. A simple model is exhibited in Fig. 6. This circuital model considers a dark current which depends totally on the gap conductivity before photo-generation, in Fig. 6 it is sketched by the impedance Z_{st}. Here UTC takes the advantage resulting from its intrinsic region that increases the resistance to the current flow through the PCA. Through the time of the transient process we could characterize the transient impedance in the circuital model as a parallel combination between a resistance and a capacitor. These two circuital elements suffer from an evolution in time in which the resistance reduces its value while the capacitor increases its own one. The energy supplied by the external electric source can be calculated as follows,

$$W_{DC} = V_0 \left(I_{DC} \nu_\gamma^{-1} + \int_0^{\nu_\gamma^{-1}} I(t) dt \right) \tag{18}$$

In Section 5 we examine, by using results, the screening effect and its interpretation by means of a circuital point of view.

5. Result

The results demonstrate the dependence of the maximum current achieved, under the same laser and bias conditions, on the charge carriers type which mainly composes the current and ultimately on the device design. In the case of direct bias, the current is mainly contributed by electrons, which is due to the fact that the photogeneration takes place close to the cathode and the distance traveled by the heavy holes is quite shorter than the one for electrons. In this way the electrons have to cross the entire gap while the holes keep close to the cathode. In the opposite case, the bias is such that the photogeneration occurs close to the anode. Then the main charge carriers are the holes. They travel through the gap whereas the electrons remain close to the anode and go into it. This explains why the current in direct bias is higher than inverse bias for all simulations as it can be seen in Figs. 7 and 8. The screening effect occurs faster over time for a device driven by electrons than for holes. This justifies why, in normalized photocurrents at high frequencies, more than 1 THz, the inverse photocurrents keep up above the direct photocurrents. However, the direct photocurrents have greater amplitudes than the ones which correspond to inverse photocurrents. This is added together with the importance of the doping distribution and the design so as to minimize the screening effect and generate higher photocurrents, which makes UTC PCAs and in particular the vertical ones the most efficient.

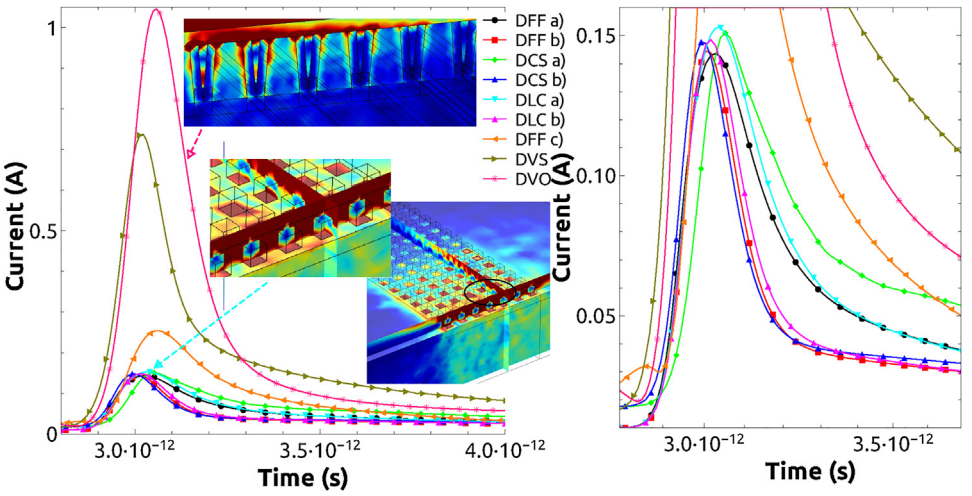

Fig. 7. Photocurrent which flows through the gap over time.

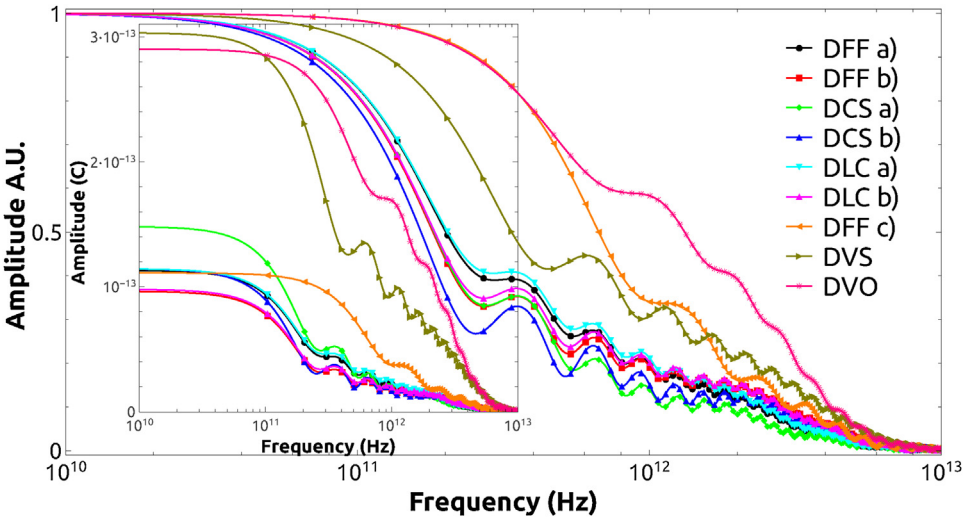

Fig. 8. Fourier transform of the photocurrent which flows through the gap.

Of course, the role played by the plasmonics effect can be clearly understood as an enhancement in the electric field distribution in the semiconductor at the optical frequency, and their effect on the amount of the photocurrent generated in the gap is evident. This is proved by simulations DCS (a) and DLC (a) in direct bias when compared with simulation DFF (a) also in direct bias. However, when compared with UTC, the plasmonics effect stays in the background. The planar UTC PCA accomplishes the best result for all planar PCAs and, when plasmonics effect and vertical structure are added, we find very high levels of intensities of current, i.e. simulation DVO. And of course, UTC, combined with both plasmonics effects and matched impedance at the laser frequency, leads to the highest photocurrent levels, as simulations DVO show in Fig. 7 and 8.

The improvement occurs in both domains-time and frequency. Considering the second term in Eq. (18), $\int_0^{\nu_\gamma^{-1}} I(t)dt$, results prove that vertical structures get more energy from the external source of voltage than the laser. Obviously, in terms of efficiency, this is a desirable result. Nevertheless it is necessary to weigh up the importance of the screening effect in the frequency distribution. In receivers based on UTC-PCA the 3-dB bandwidth, $f_{3\text{dB}}$ can be expressed as $f_{3\text{dB}} = \frac{1}{2\pi\sqrt{\tau_{tr}^2+\tau_{RC}^2}}$ [31].

The UTC decreases the transit time τ_{tr} but the RC time should be decreased too in order to reach higher cut off frequencies $f_{3\text{dB}}$. The most surprising evidence from the results in Fig. 9 is the non-intuitive capacitance $C(t)$ when we think in a parallel plate capacitor (where $C = \frac{\varepsilon A}{d}$). We can appreciate that if we compare $C(t)$, for instance, for both DCS simulated, at frequencies above 2 THz the photocurrent of DCS (a) runs beneath DSC (b) as can be seen in Figs. 8 and 9. This is an incredible result which is partially explained by the shorter screening growth in time accomplished for electrons which rise the capacitance of the device over time faster than the one due to holes.

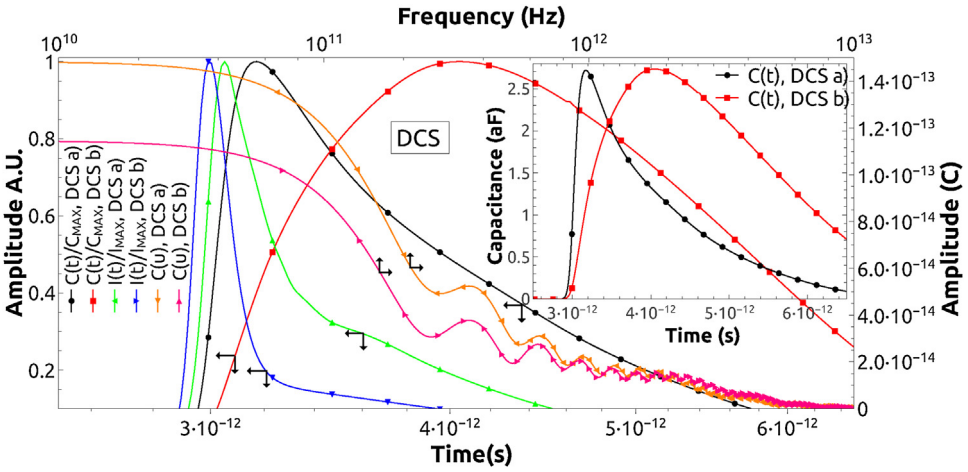

Fig. 9. The big figure (top-right axes) shows the frequency composition of the photocurrents for both simulations carried out, DCS (a) and DCS (b). The small figure shows the capacitance over time. The big figure also depicts the normalized capacitance (top-left axes) together with the normalized photocurrent (bottom-left axes) over time for both simulations DCS (a) and DCS (b).

6. Conclusions

The results have yielded a simple conclusion, in the efficiency of a PCA it is possible to make strides by combining several aspects. Indeed, these aspects bring about improvements in two specific directions, on one hand the laser absorption and on the other hand, reduction of the transit time which charge carriers need so as to cross the gap. We can also conclude that simulations applied to designs are an essential tool in screening effect control and save time, money and resources.

We have found out that properly biased vertical UTC PCAs, in which the impedance between the air and the semiconductor is matched at laser wavelength, achieve the best performance. Under the same laser conditions and external bias voltage, a good design is very important. Also, the DVO design leads to the best performance. It generates more intensity of current in the highest frequencies. In conclusion, in the design of a PCA it is vital to keep in mind four elements which can be summarized as follows: the bias direction, the distribution doping in the semiconductor, the plasmonic effects, the matching of impedance at laser frequency and last but no least, to illuminate the PCA in the same direction as the photocurrent flow.

Acknowledgements

The first author would like to thank Juan Bautista Roldán Aranda at the University of Granada for his review of this manuscript. The second author would like to thank Zahra Hemmat for her help.

References

[1] Comsol Multiphysics, https://www.comsol.com/.
[2] C.M. Armstrong, The truth about terahertz, IEEE Spectr. 49 (9) (2012) 36–41.
[3] E. Moreno, Z. Hemmat, J.B. Roldán, M.F. Pantoja, A.R. Bretones, S.G. García, Time-domain numerical modeling of terahertz receivers based on photoconductive antennas, J. Opt. Soc. Am. B 32 (10) (2015) 2034–2041.
[4] E. Moreno, Z. Hemmat, J.B. Roldán, M.F. Pantoja, A.R. Bretones, S.G. García, R. Faez, Implementation of open boundary problems in photo-conductive antennas by using convolutional perfectly matched layers, IEEE Trans. Antennas Propag. 64 (11) (2016) 4919–4922.
[5] S.H. Yang, M.R. Hashemi, C.W. Berry, M. Jarrahi, 7.5% optical-to-terahertz conversion efficiency offered by photoconductive emitters with three-dimensional plasmonic contact electrodes, IEEE Trans. Terahertz Sci. Technol. 4 (5) (2014) 575–581.
[6] S. Lepeshov, A. Gorodetsky, A. Krasnok, E. Rafailov, P. Belov, Enhancement of terahertz photoconductive antenna operation by optical nanoantennas, Laser Photon. Rev. 11 (1) (2016) 120.
[7] T. Ishibashi, Y. Muramoto, T. Yoshimatsu, H. Ito, Unitraveling-carrier photodiodes for terahertz applications, IEEE J. Sel. Top. Quantum Electron. 20 (6) (2014) 79–88.
[8] E. Moreno, M.F. Pantoja, A.R. Bretones, M. Ruiz-Cabello, S.G. García, A comparison of the performance of THz photoconductive antennas, IEEE Antennas Wirel. Propag. Lett. 13 (2014) 682–685.
[9] M.B. Johnston, D.M. Whittaker, A. Corchia, A.G. Davies, E.H. Linfield, Simulation of terahertz generation at semiconductor surfaces, Phys. Rev. B 65 (2002) 165301.
[10] C. Berry, N. Wang, M. Hashemi, M. Unlu, M. Jarrahi, Significant performance enhancement in photoconductive terahertz optoelectronics by incorporating plasmonic contact electrodes, Nat. Commun. (2012) 1–10.
[11] N. Burford, M. El-Shenawee, Computational modeling of plasmonic thin-film terahertz photoconductive antennas, J. Opt. Soc. Am. B 33 (4) (2016) 748–759.
[12] E. Moreno, M.F. Pantoja, S.G. García, A.R. Bretones, R.G. Martín, Time-domain numerical modeling of THz photoconductive antennas, IEEE Trans. Terahertz Sci. Technol. 4 (4) (2014) 490–500.
[13] P. Kirawanich, S.J. Yakura, N.E. Islam, Study of high-power wideband terahertz-pulse generation using integrated high-speed photoconductive semiconductor switches, IEEE Trans. Plasma Sci. 37 (1) (2009) 219–228.
[14] K. Yamazaki, T. Yamaguchi, H. Namatsu, Three-dimensional nanofabrication with 10-nm resolution, Jpn. J. Appl. Phys. 43 (8B) (2004) L1111.
[15] K. Yamazaki, H. Namatsu, 5-nm-order electron-beam lithography for nanodevice fabrication, Jpn. J. Appl. Phys. 43 (6S) (2004) 3767.

[16] S. Cabrini, Sub-10-nm three-dimensional plasmonic probes and sensors, 2016 Progress in Electromagnetic Research Symposium (PIERS) (2016) 836.
[17] Y. Mao, Z. Chen, J. Zhu, Y. Pan, W. Wu, J. Xu, Stereo metamaterial with three dimensional meta-atoms fabricated by programmable stress induced deformation for optical modulation, 2017 IEEE 30th International Conference on Micro Electro Mechanical Systems (MEMS) (2017) 285–288.
[18] D.A. Kleinman, The forward characteristic of the PIN diode, Bell Syst. Tech. J. 35 (3) (1956) 685–706.
[19] T. Gupta, Dielectric Materials, Springer New York, New York, NY, 2009, pp. 67–110.
[20] http://ees.elsevier.com/ijleo/download.aspx?id=257275&guid=bec2076a-4c82-4728-844e-342e72540452&scheme=1.
[21] E. Sano, T. Shibata, Fullwave analysis of picosecond photoconductive switches, IEEE J. Quantum Electron. 26 (2) (1990) 372–377.
[22] B.E.A. Saleh, M.C. Teich, Fundamentals of Photonics, Wiley, 2007.
[23] RP Photonics Encyclopedia https://www.rp-photonics.com.
[24] K.M. McPeak, S.V. Jayanti, S.J.P. Kress, S. Meyer, S. Iotti, A. Rossinelli, D.J. Norris, Plasmonic films can easily be better: rules and recipes, ACS Photon. 2 (3) (2015) 326–333.
[25] D.E. Aspnes, A.A. Studna, Dielectric functions and optical parameters of Si, Ge, GaP, GaAs, GaSb, InP, InAs, and InSb from 1.5 to 6.0 eV, Phys. Rev. B 27 (1983) 985–1009.
[26] D.E. Aspnes, S.M. Kelso, R.A. Logan, R. Bhat, Optical properties of AlxGa1 − x As, J. Appl. Phys. 60 (2) (1986) 754–767, http://dx.doi.org/10.1063/1.337426.
[27] L. Gao, F. Lemarchand, M. Lequime, Refractive index determination of SiO_2 layer in the UV/Vis/NIR range: spectrophotometric reverse engineering on single and bi-layer designs, J. Eur. Opt. Soc. (2013), http://dx.doi.org/10.2971/jeos.2013.13010.
[28] SILVACO International, ATLAS User's Manual DEVICE SIMULATION SOFTWARE, 2006, 4701 Patrick Henry Drive, Bldg. 1 Santa Clara, CA 95054.
[29] M. Levinshtein, S. Rumyantsev, M. Shur, Handbook Series on Semiconductor Parameters: In 2 Volumes, 1996.
[30] D.C. Look, Molecular beam epitaxial GaAs grown at low temperatures, Thin Solid Films 231 (1) (1993) 61–73.
[31] B. Banik, J. Vukusic, H. Hjelmgren, J. Stake, Optimization of the UTC-PD epitaxy for photomixing at 340 GHz, Int. J. Infrared Millimeter Waves 29 (10) (2008) 914–923.